

Enhanced Carrier Transport Distance in Colloidal PbS Quantum-Dot-Based Solar Cells Using ZnO Nanowires

Haibin Wang,[†] Victoria Gonzalez-Pedro,^{*,‡} Takaya Kubo,^{*,†} Francisco Fabregat-Santiago,[‡] Juan Bisquert,^{‡,§} Yoshitaka Sanehira,[†] Jotaro Nakazaki,[†] and Hiroshi Segawa^{*,†}

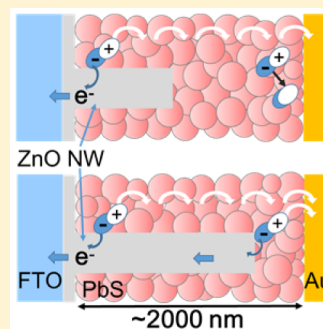
[†]Research Center for Advanced Science and Technology, The University of Tokyo, 4-6-1 Komaba, Meguro-ku, Tokyo 153-8904, Japan

[‡]Institut of Advanced Materials (INAM), Universitat Jaume I, 12006 Castellón, Spain

[§]Department of Chemistry, Faculty of Science, King Abdulaziz University, Jeddah, Saudi Arabia

Supporting Information

ABSTRACT: Nanostructured solar cells are a promising area of research for the production of low cost devices that may eventually be capable of complementing or even replacing present technologies in the field of solar power generation. The use of quantum dots (QDs) in solar cells has evolved from being simple absorbers in dye-sensitized solar cells to sustaining the double functions of absorbers and carrier transporters in full solid state devices. In this work, we use both optical and electrical measurements to explore the diffusion limitations of carrier transport in cells made of a heterostructure combining lead sulfide (PbS) QDs as absorbers and hole carrier and zinc oxide nanowires as electron carrier material. The results show efficient charge collection along the PbS-QD/ZnO nanowire (NW) hybrid structure. This is because of the formation of band bending in the ZnO collector, allowing efficient charge separation and spatially well-separated carrier pathways, yielding a hole transportation of over 1 μm . We have also found a limitation in open-circuit voltage (V_{oc}) associated with band bending in the ZnO collector.



INTRODUCTION

Nanostructured wide band gap semiconducting materials are attractive for their use in optoelectronic devices such as photovoltaic solar cells and light-emitting diodes. Among various wide band gap semiconductors, TiO_2 ¹ and ZnO ² are useful electron transport and electron-selective contact materials in next-generation photovoltaics because of their high carrier mobility, high dielectric constants, and energy levels. In this regard, highly crystalline ZnO nanostructures are good candidates because of their large diffusion coefficients, which allow them to reach diffusion lengths of up to 1 μm ,³ and their mild growth procedures using solution-processed methodologies such as hydrothermal synthesis,⁴ spray pyrolysis deposition,⁵ and so forth.⁶ Different 1-D ZnO templates including nanowires (NWs), rods, and tubes have been implemented in organic, dye-sensitized,^{7,8} and thin-film solar cells,⁹ aiming at establishing good electron pathways. Nanostructured wide band gap metal oxides have also been exploited in colloidal quantum dot (QD)-based solar cells,¹⁰ wherein the nanostructure control is an important challenge to increase carrier transport efficiency.^{11,12} In this context, Jean et al. reported PbS-QD/ ZnO -NW-based heterojunction solar cells and achieved an external quantum efficiency (EQE) value of approximately 25% in the near-infrared (IR) region.¹³ Sargent and collaborators used well-ordered TiO_2 nanopillars¹⁴ to construct PbS-QD/ TiO_2 rod-based heterojunction solar cells. In previous research we reported on PbS-QD-based heterojunction solar cells that employed

ZnO -NWs as charge separators and carriers.¹⁵ The morphology of ZnO -NW arrays was systematically investigated to achieve high light-harvesting efficiency (LHE) as well as efficient carrier collection. The solar cells with PbS-QD/ ZnO -NW bulk heterojunction (BHJ) structures made up of densely grown thin ZnO -NWs approximately 1200 nm long yielded a maximum EQE of approximately 60% in the near-IR region (at 1020 nm) and over 80% in the visible region and long-term stability under continuous light soaking.¹⁶ Furthermore, Chang et al. showed that the passivation of the ZnO surface provides a very large boost of photovoltage by decreasing recombination.¹⁷

Nevertheless, the carrier transport properties of PbS-QD films as well as of the ZnO PbS blend have not been elucidated in detail. Several carrier transport mechanisms in PbS and PbSe solid films have been proposed, which include thermally activated carrier transport¹⁸ and tunneling transport based on Miller–Abrahams formalism.¹⁹ It is necessary to unveil diffusion mechanisms in solar cells mainly because the carrier transport properties of QD solid films depend on the choice of ligands,^{20,21} QD size distributions,²⁰ QD packing density,²² and density of trap states closely related to surface passivation.^{23,24}

In this paper, we have studied the optoelectronic properties of PbS-QD/ ZnO -NW solar cells by focusing on their solar cell

Received: September 19, 2015

Revised: October 28, 2015

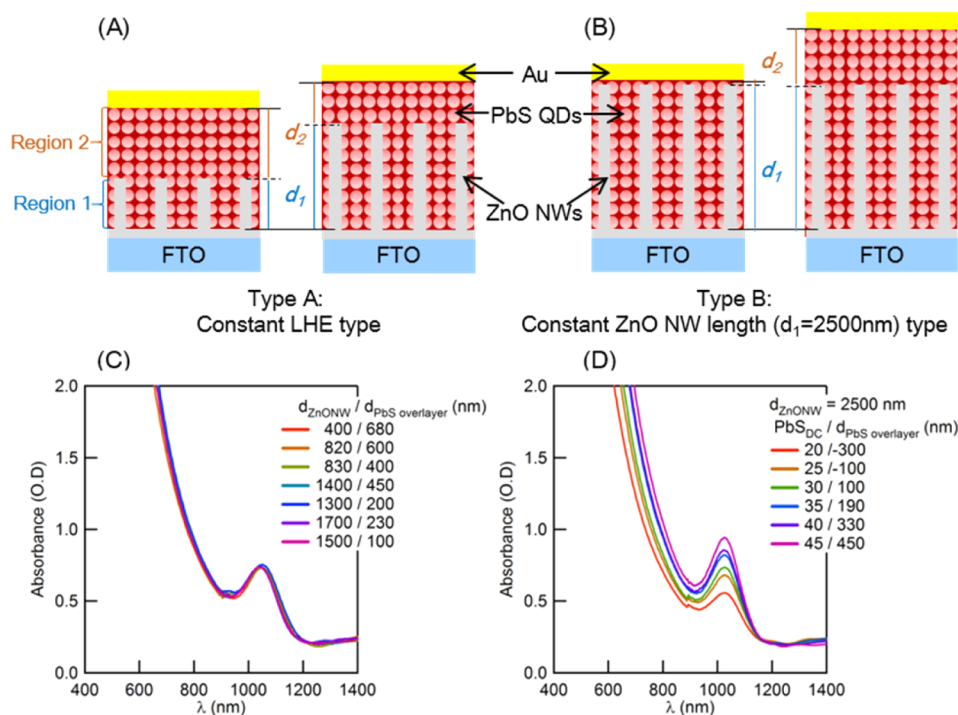


Figure 1. Schematic of the PbS-QD/ZnO-NW solar cells and their respective absorbance spectra. (A, C) Type A cells: the d_2 (PbS overlayer thickness) is adjusted to keep LHE constant. (B, D) Type B cells: d_1 , ZnO-NW length, is a constant of 2500 nm, and d_2 changes as a function of number of PbS-QD deposition cycles. The solar cell structure is divided into two different regions, the PbS-QD/ZnO-NW (region 1) and PbS bulk overlayer (region 2).

structure. We confirmed the importance of ZnO-NWs as n-type electron collectors. We also observed two differentiated transport mechanisms related to the PbS ZnO-NW blend region and bulk PbS overlayer. The transport limitation in the latter will determine the final photocurrent in the device. The most important finding is that, once good electron pathways are established in the PbS-QD/ZnO-NW BHJ structure, transport losses are reduced, and the absorbed photons are efficiently converted to photocurrent. In these conditions, holes in the PbS can diffuse a distance of over 1000 nm or longer.

EXPERIMENTAL METHODS

PbS-QD-based BHJ solar cells were constructed by combining ZnO-NW arrays with PbS-QDs, whose first absorption peak was at wavelengths longer than 1000 nm. The ZnO-NW arrays with different thicknesses were formed on dense ZnO seed layers by a hydrothermal method.¹⁶ The PbS-QDs were infiltrated into the ZnO-NW array from a PbS-QD octane solution (50 mg mL⁻¹) using the layer-by-layer spin-coating method. The deposited PbS-QD layers were treated with a cetyltrimethylammonium bromide (CTAB)-methanol (10 mg mL⁻¹) solution to replace insulating oleic acid chain ligands with bromide anions.²¹ The substrates were then rinsed with a methanol solution to remove excess CTAB and oleic acid ligands. After the ZnO array was infiltrated with PbS-QDs, an additional PbS overlayer was deposited by the spin-coating method. Here we constructed two types of solar cells (Figures 1A and 1B and Supporting Information (SI) Figure S1–3, referred to as Type A and B, respectively). The thickness of the overlayers in the Type A solar cells was adjusted to keep the exciton absorption intensity constant, thereby maintaining an equal LHE (Figure 1C). Therefore, the thickness of the PbS overlayer decreased with increasing ZnO-NW length. All the spin-coating processes were performed at a humidity of approximately 50 RH% or lower.

Finally, a Au back contact was deposited on top of the PbS-QD overlayer by thermal evaporation. Two different batches of ZnO-NW arrays were used to construct type A cells with different average NW diameter, which contributed to the scattered data plots. (ZnO-NW lengths of (a) 400, 830, 1300, and 1500 nm and (b) 820, 1400, and 1700 nm are shown in SI Figure S1 and Table S1.) The PbS-QD-based solar cells of Type B with 2500 nm thick ZnO-NW arrays were constructed by depositing PbS overlayers with different PbS-QD deposition cycles (Figure 1D, SI Figure S2).

The photovoltaic performance of the cells was evaluated by measuring current density–voltage (J – V) curves from which open-circuit voltage (V_{oc}), short-circuit current density (J_{sc}), fill factor (FF), and PCE were obtained. J – V curves were measured under simulated AM1.5G filter irradiation (100 mW cm⁻²) using a class A solar simulator (Bunko-keiki, CEP-2000MLQ). All solar cells were fabricated and measured in air. The EQE spectra were measured from 300 to 1500 nm (Bunko-keiki, CEP-2000MLQ). Complex impedances of the solar cell were measured in the frequency range between 1 MHz and 1 Hz using a potentiostat and a frequency analyzer (Solartron, SI1260). IMPS (intensity-modulated photocurrent spectroscopy) measurements were carried out by modulating the intensities of the incident beams (at 590 nm, 18 mW cm⁻²) with a ModuLab MX PhotoEChem (Solartron, ModuLab), where the modulation amplitude was 5% of the incident light intensity and the modulation frequency was varied from 100 kHz to 1 Hz.

RESULTS AND DISCUSSION

PbS-QD-based BHJ solar cells were constructed by infiltrating ZnO-NW arrays with PbS-QDs from a PbS-QD octane solution by the layer-by-layer deposition method.^{15,16} Two different configurations were used to build the solar cells: In Type A cells, shown in Figure 1A, the length of the ZnO-NWs (d_1) was

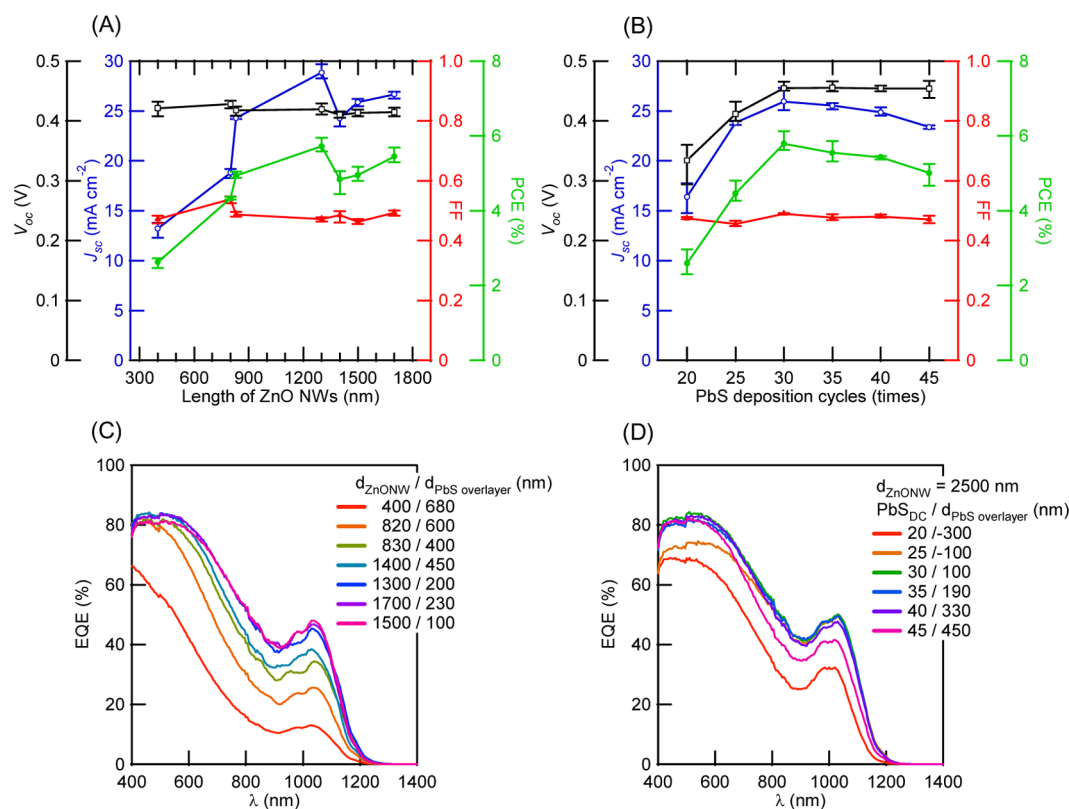


Figure 2. Solar cell performances. J_{sc} (green ○), V_{oc} (black □), FF (red ▲), and PCE (green ●) for PbS-QD/ZnO-NW solar cells fabricated with different ZnO-NW lengths (A) and different PbS deposition cycles (B), and respective EQE spectra ((C) and D)).

variable, while the thickness of the PbS-QDs overlayer (d_2) was adjusted to keep the absorbance constant (see Figure 1C). In Type B PbS-QD/ZnO-NW BHJ cells, the thickness of ZnO-NWs (d_1) was kept constant (2500 nm), while that of the PbS overlayer was varied (d_2), as indicated in Figure 1B.

In Type A cells the thickness of the PbS overlayer reduced with increasing ZnO-NW length (see cross-sectional scanning electron microscopy (SEM) images in SI Figure S1 and Table S1), indicating a good adsorbance for the PbS-QDs embedded in the NWs. The ratio of the NW thickness and PbS overlayer was chosen such that LHE remained constant (Figure 1C). The Type B solar cells were constructed controlling the number of PbS-QDs loaded over the 2500 nm long ZnO-NW array by controlling the number of PbS-QD deposition cycles. The cross-sectional SEM images of the resulting cells are shown in SI Figure S2. In this type of cell, the LHE increases with the number of PbS-QD deposition cycles (PbS_{DC}), as Figure 1D shows. Note that for a number of cycles smaller than 30 a PbS overlayer is not observed, suggesting incomplete filling of the ZnO-NW pores. The LHE spectra (SI Figure S4) of the cells were calculated from the absorbance spectra of the cells without the Au back contact (A_{Total}) after correcting from light losses in the FTO (F-doped SnO_2) substrate (A_0) (SI eq S5 and Figure S3).

The short-circuit current density (J_{sc}), open-circuit voltage (V_{oc}), fill factor (FF), and power conversion efficiency (PCE) obtained for the solar cells were plotted as a function of the length of the ZnO-NWs in Type A cells (Figure 2A) and the number of PbS deposition cycles in Type B cells (Figure 2B).

The EQE spectra of the Type A solar cells depended on the ZnO-NW length despite the similar LHE shown in Figure 2C. The solar cell with 400 nm long ZnO-NWs gave an EQE of

13% at the low-energy absorption peak observed at 1020 nm. The EQE value increased as the ZnO-NWs became longer and reached a maximum of 48% in the solar cell with 1500 nm long ZnO-NWs. Accordingly, J_{sc} increased with thicker ZnO-NWs and reached a maximum value at 1300 nm (28 mA cm^{-2}), approximately twice the value obtained for the 400 nm long ZnO-NWs (14 mA cm^{-2}). The photocurrent was in reasonably good agreement with the maximum photocurrent extracted by the integration of EQE spectra and multiplied by the photon flux in the relevant wavelength range (27.1 mA cm^{-2}). In addition, it represents 81% of the maximum theoretical current that could be obtained with this absorber ($E_{gap} = 1.18 \text{ V}$, $J_{max} = 34.45 \text{ mA cm}^{-2}$). Although close observation of V_{oc} behavior shows a slight decrease in V_{oc} , the values were virtually constant about 0.42 V for the ZnO-NW lengths employed. Similar behavior in the EQE was observed for the solar cells fabricated with different PbS deposition cycles and fixed with 2500 nm thick ZnO-NWs (Type B cells, Figure 2D). In this set, for the cells with incomplete filling of ZnO-NWs, both V_{oc} and J_{sc} decreased with decreasing PbS layer thickness. This is attributed mainly to the thinner PbS overlayer and to a lesser degree to the lower PbS content or the direct contact between the gold contact and the ZnO-NW, producing a new path for charge losses. Once pores were filled V_{oc} remained constant, while J_{sc} decreased with increasing overlayer thickness. Therefore, we can conclude that while the increase in the PbS-QD/ZnO-NW BHJ region helped cell optimization thick PbS overlayers decreased the cell performance in general.

Figures 3A and 3B show the IQE spectra of Type A and B solar cells, respectively, which were estimated from the quotient between the EQE and LHE after correcting for the transmittance of the FTO substrate (SI eq S5). In the case of Type A devices,

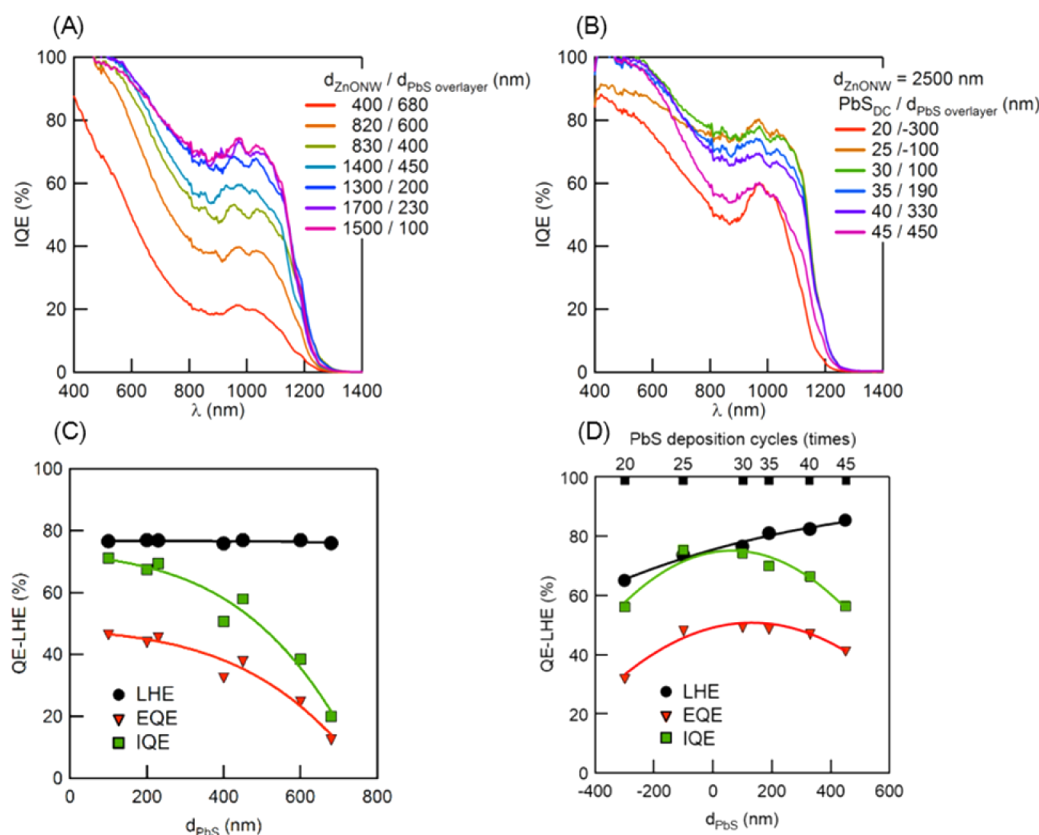


Figure 3. Internal quantum efficiency spectra. (A) IQE spectra of PbS-QD solar cells with different ZnO-NW lengths and (B) PbS deposition cycles. IQE spectra were extracted from a quotient between the EQE (Figure 2C, 2D) and LHE (SI Figure S4) after correcting from the transmittances of FTO substrate. (C) and (D) EQE, IQE, and LHE versus PbS overlayer thickness at fixed wavelength ($\lambda = 1020$ nm).

despite the similar LHEs the IQE increased with the ZnO-NW length (d_{ZnONW}) (Figure 3C).

Note that, in both types of cells, the quantum efficiencies are 100% in the visible region and near 80% at the absorption peak (at 1020 nm) for thinner PbS overlayers ($d_{\text{PbS}} < 200$ nm). Therefore, the transport losses were not relevant in those devices, and thus, most of the absorbed photons were efficiently converted to electricity. However, IQE decreased continuously for thicker PbS overlayers (Figure 3C). This indicates that the collection efficiency was directly affected by the short diffusion length of the photocarriers in the bulk PbS and that the photoconversion efficiency is dominated by the thickness of the overlayer. Paying attention to the IQE, the diffusion length in the colloidal QD film was expected to be shorter than 200 nm, which correlated with the reported values of $L_D = 80 \pm 10$ nm.²⁵ Henceforth, the combination of efficient absorber materials with long diffusion n-type contacts may be considered a good route for designing highly efficient solid state solar cells.

For further insight into the experimental results we used the model schematized in Figure 4A, wherein the PbS-QD/ZnO-NW BHJ region and PbS bulk overlayer are treated separately and constitute two differentiated regions with different recombination rates and lifetimes. This approach allows expressing the total EQE as the sum of partial contributions from the blend region and PbS overlayer

$$\text{EQE}_{\text{Total}}(\lambda) = \frac{J_{\text{sc}}(\lambda)}{q\Phi_{\text{in}}(\lambda)} = T_0 \text{IQE}_{\text{BHJ}} \cdot \text{LHE}_{\text{BHJ}} + \text{EQE}_{\text{PbS}} \quad (1)$$

Therefore, as further described in the SI Note S1, the contribution to EQE from the PbS overlayer (EQE_{PbS}) could be estimated by predicting the EQE of BHJ from FTO transmittance (T_0) and blend heterojunction IQE and LHE and subtracting this contribution from the total quantum efficiency (see Figure 4B and 4C). In all of the studied cells, thick PbS overlayers produced negative values of EQE_{PbS} , particularly at long wavelengths. The exception to the trend occurred for a Type A cell with 400 nm ZnO-NW, which was unable to absorb all low wavelengths within the blend, and the QD unfilled Type B cells ($d_{\text{PbS}} = -300$ nm, -100 nm), again for their difficulties in harvesting all of the light received.

The drop in EQE_{PbS} was observed for cells with PbS overlayers thicker than 230 nm. The negative values of the EQEs were ascribed to carrier losses in the PbS overlayer related to its short diffusion length mentioned above. The consequence of these losses is a decrease in J_{sc} and PCE as shown in Figure 2A and 2B.

Note that in the cases of cells comparable on the basis of PbS overlayer thickness, such as 830/400, 1400/450, and 1300/200, the cells with the thinner BHJ region presented much larger losses. This was because the thicker ZnO-NWs enhanced the light harvesting in the blend region, where charge collection was more efficient, and because the generation of photocarriers in the bulk PbS was reduced, which resulted in the lower charge losses. Type B devices, while following the same trend, produced higher losses in EQE_{PbS} . The origin of this behavior is associated with the fact that these cells presented a smaller absorption coefficient at the BHJ layers. Thus, well-differentiated cells, such as 1400/450 (Type A) and 2500/450 (Type B), presenting similar LHEs and a continuous rise in LHE in Type B cells with

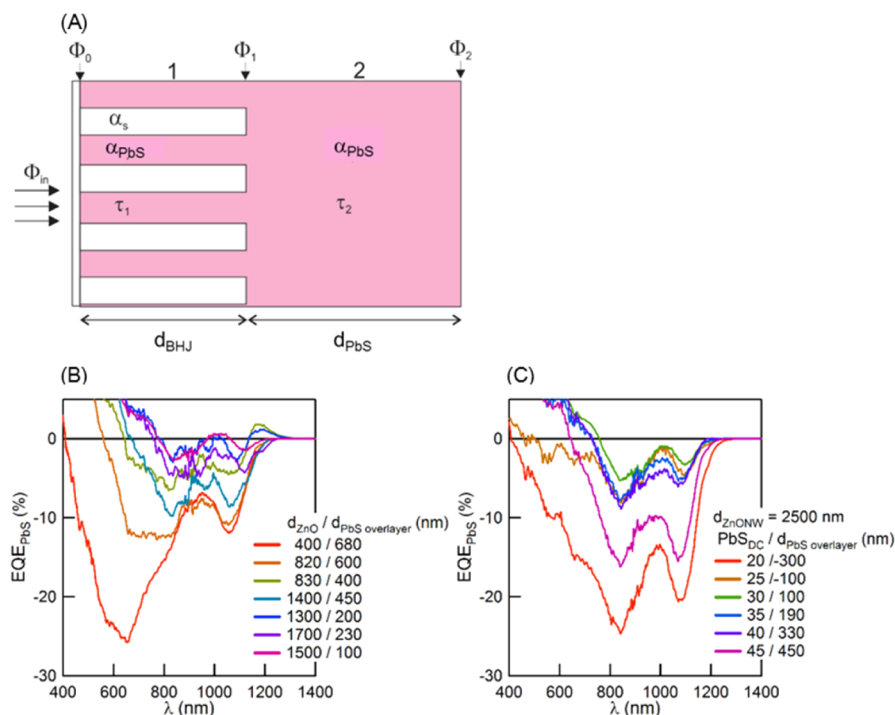


Figure 4. (A) Scheme of theoretical model to describe the quantum efficiency in terms of the parts of the device. Bottom: EQEs of PbS-QD bulk overlayer (region 2) in the solar cells with different ZnO-NW lengths (B) and PbS deposition cycles (C).

increasing overlayer thicknesses gave evidence of smaller light absorption in the BHJ layer made with 2500 nm long NWs (see also the absorption coefficient calculations in SI Note S1 and Figure S5). This implies that PbS-QDs found more difficulties in penetrating ZnO-NWs that were too long.

These experimental observations clearly showed that the introduction of ZnO-NWs promotes charge separation and indicated that the diffusion length in the PbS overlayer was a limiting parameter in solar power generation. Therefore, in either case, the thickness of the PbS overlayer should be as thin as possible to achieve high efficiency solar cells but sufficient to enable an adequate contact with gold to prevent short circuit with ZnO-NWs.

Impedance spectroscopy (IS) is a powerful tool for studying the carrier transport properties of PbS-QD solar cells.^{26–31} IS was applied to the PbS-QD/ZnO-NW solar cells, testing different mesostructured and PbS thicknesses. Characteristic Nyquist plots of Type A solar cells obtained in the dark at a bias voltage of 0.3 V and under illumination at 0 V are depicted in Figure 5A and 5B. Impedance data could be fitted with the equivalent circuit model of Figure 5C. In this circuit we discriminated the impedance response of the PbS-QD/ZnO-NW BHJ (Z_{BHJ} for region 1) and the bulk PbS overlayer (Z_{G} , for region 2). Z_{BHJ} includes the effect of transport in the PbS-QDs and ZnO-NWs together with the effects of internal polarization and charge recombination losses between QDs and NWs. This can be approached through a transmission line model as in SI Figure S6.

However, for most of the situations, the parallel combination $R_{\text{BHJ}} - C_{\text{BHJ}}$ (or $R_{\text{BHJ}} - \text{CPE}$) is the most accurate circuit that may be used to fit the data. When the PbS overlayer is large, Z_{G} fits reasonably well with the Gerischer impedance³²

$$Z_{\text{G}} = \frac{R_{\text{G}}}{(1 + i\omega/\omega_{\text{rec}})^{1/2}} \quad (2)$$

with ω_{rec} being the recombination frequency and R_{G} providing the DC limit of the PbS overlayer resistance.

Under dark conditions, as shown in Figure 5A, the overlap between medium and low frequency (MF and LF, respectively) arcs depends on the conditions of potential for the measurements and the relative thicknesses of regions 1 and 2 of the solar cell. The observed trend followed the rule that the thicker the layer, the lower the characteristic frequency of its impedance. This may be associated with the increasing contribution of transport resistances in Z_{G} and Z_{BHJ} . As a consequence of this behavior, it was not possible to specifically assign the MF and LF arcs to one of these contributions, making it more complex to obtain an accurate fit of the data.

The impedance model needs to be completed with the contributions from contacts, as described in the SI Figure S6. The complexity of the interactions that contributed to the total impedance of the cell and the large overlap observed in the MF and LF arcs for most of the cells made it convenient to follow a simplified approach for the treatment of data. Thus, we first focused on the total DC resistance (R_{DC}) of different cells taken under illumination at different forward potentials plotted in Figure 6. As can be observed, the thicker films presented the larger total resistance, which may be attributed to the contribution of transport resistances in the different regions. The opposite case, with recombination resistance dominating the changes in R_{DC} , would produce a decrease in its value. Focusing on the Type B cells with 2500 nm thick region 1, Figure 6 shows that at low potentials R_{DC} was the same in both cells and very close to the values of the thinner Type A cells (1500/100). This indicates that at these potentials R_{DC} is dominated by the contribution from the BHJ region together with a relevant charge transfer at the interfaces (R_{HF}). At higher potentials, R_{DC} in Type B cells with thicker overlayers (450 nm) showed a larger value than the cell with a thin PbS overlayer (100 nm). This difference (ΔR_{G}) was directly

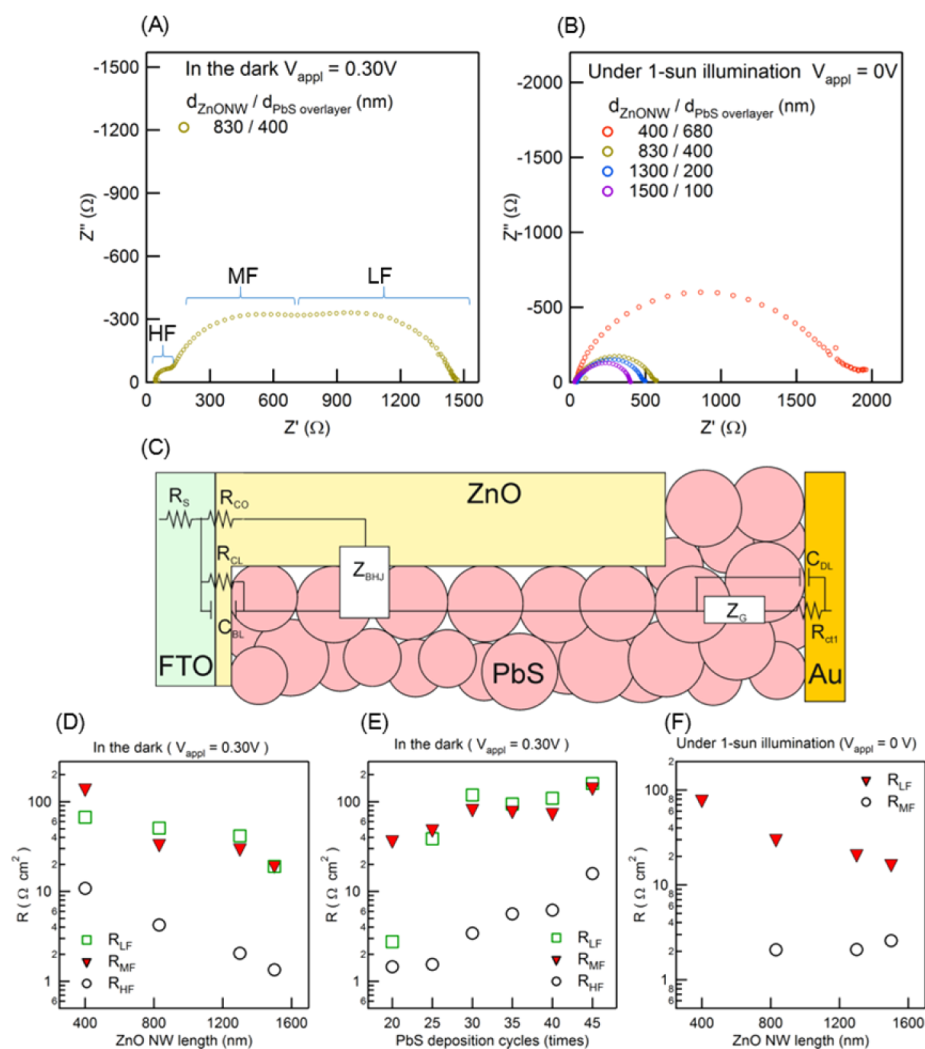


Figure 5. Impedance spectroscopy spectra. Typical Nyquist plots obtained on the PbS-QD/ZnO-NW solar cell (A) in the dark and (B) under illumination (100 mW cm^{-2} ; at $20 \text{ }^\circ\text{C}$). (C) Proposed equivalent circuit model used to fit impedance data. R_s accounts for the series resistance contribution because of FTO, gold wires, and contacts; R_{ct1} and R_{ct2} account for the charge transfer from FTO to ZnO-NWs and from gold to PbS-QD, respectively; C_{DL} accounts for interfacial capacitance at the ZnO back layer; C_{DL} is the double-layer capacitance at the gold PbS-QD interface; Z_{BHJ} accounts for the impedance at the PbS-QD/ZnO-NW BHJ region; and Z_G represents the impedance of the bulk PbS-QD overlayer which is given by a Gerischer impedance. Resistance values at the different frequency regions ($R_{HF} = R_{ct1} + R_{ct2}$, $R_{MF} = R_{BHJ}$, $R_{LF} = R_G$) in the dark at 0.3 V as a function of (D) ZnO-NW length and (E) the number of PbS deposition cycles. (F) Resistances obtained under illumination as a function of ZnO-NW length. Note that under illumination MF and LF arcs merge in a single one that cannot be distinguished, and thus the equivalent $R_{LF} = R_{BHJ} + R_G$ is represented.

attributable to the 350 nm layer difference in the PbS bulk region 2.

For Type A cells, the differences in R_{DC} for the ratios 1500/100 nm and 830/400 nm between the blend and overlayer were minimal. However, we used data from the Type B cells to have a closer look at the reasons for these similarities. Thus, by normalizing the variations of R_G to the overlayer thickness, we could obtain a rough estimation of R_{BHJ} in the blend. Recalculating these values for the sizes of blend and overlayer in Type A cells and considering the porosity of the blends (SI Tables S1 and S2) we obtained the dashed lines plotted in Figure 6. The differences observed between this estimation and the real values were minimal and restricted to the case of the thinner blend (830/400) at low potentials. These differences were attributable to the contribution from charge transfer at the contacts, which was not considered for normalization. At low potentials this difference is larger, in good agreement with the fact that these potentials' interfacial charge transfer R_{HF} contributed to R_{DC} as described

above. At high potentials the interfacial contribution diminished, and simulated and real R_{DC} of 1500/100 nm and 830/400 nm cells matched again, as the lower contribution from R_{BHJ} in the 830 nm region is compensated for by the larger R_G attributable to the 400 nm PbS overlayer. These results, together with the apparition of a Gerischer impedance in the Nyquist plots of thick PbS layers, confirmed that the carrier harvesting in the heterojunction layer took place more efficiently than in the PbS overlayer.

The fitting of the impedance data provided similar results to those obtained in the analysis conducted so far. Thus, the contribution from both the PbS-QD/ZnO-NW BHJ, R_{BHJ} , and from the PbS overlayer thickness, R_G , decreased as their respective regions became thinner (Figures 5D and 5E). Unlike the Nyquist plots taken in the dark, those obtained in the short-circuit condition and under 1 sun illumination (Figure 5) showed a large single arc wherein MF and LF arcs merged. The equivalent

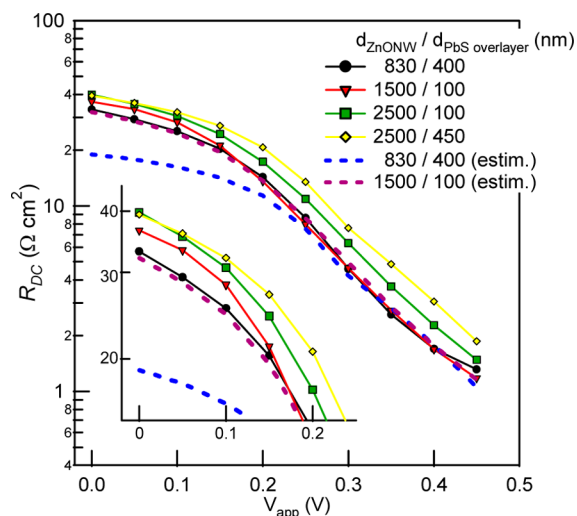


Figure 6. DC resistance of cells with different ZnO-NW/PbS-QD overlayer thickness ratios. Dashed lines represent the estimation of cells 830/400 and 1500/100 from data with 2500/100 and 2500/450.

($R_{LF} = R_{BHJ} + R_G$) was quite stable with increasing ZnO-NW length (Figure 5F).

Mott–Schottky plots of high frequency capacitance C_{HF} for four configurations are shown in Figure 7, showing a reasonable

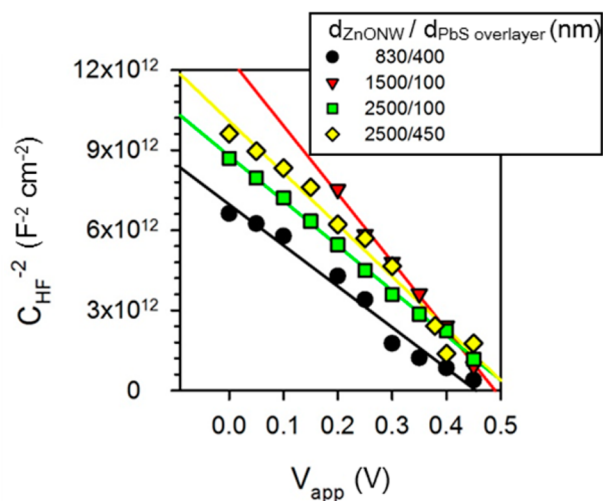


Figure 7. Mott–Schottky plots of interfacial capacitances in several PbS-QD/ZnO-NW solar cells obtained under illumination.

agreement between the cells. The data obtained indicate a depletion region larger than PbS-QD, with a doping density of $\sim 10^{17} \text{ cm}^{-3}$, agreeing well with the values obtained for annealed ZnO³³ and which was therefore attributed to the compact layer of ZnO. Parameters are summarized in Table 1. The depletion region is always smaller than 32 nm that is smaller than the compact layer size and even close to the radius of the ZnO-NWs.

Summarizing these results, ZnO acted as a very efficient charge separator and collector for the electrons absorbed in PbS-QD base.

Intensity-modulated photocurrent spectroscopy (IMPS) is a direct technique for studying photocurrent processes taking place at different time domains at different layers and interfaces. IMPS spectra measured on four different PbS-QD/ZnO-NW solar cells were composed of two semicircles in the first quadrant

Table 1. V_{oc} and Parameters Obtained from Mott–Schottky Plots in Figure 7 for Cells with Different Region 1/Region 2 Ratio^a

cell	V_{oc} (V)	V_{fb} (V)	N_d (cm^{-3})	w (nm)
830/400	0.41	0.46	9.2×10^{17}	24
1500/100	0.41	0.49	5.5×10^{17}	32
2500/100	0.43	0.52	8.4×10^{17}	26
2500/450	0.43	0.52	7.3×10^{17}	28

^a V_{fb} stands for flat band potential, N_d donor for carrier density, and w for depletion region (calculated at 0.5 V below flat band conditions).

(Figure 8A). The solar cell with 400 nm long ZnO-NWs showed two distinct semicircles (red line). The one appearing on the low frequency side (I_{LF}) was assigned to the carrier dynamics related to the PbS layer and the one on the high frequency side (I_{HF}) to the PbS-QD/ZnO-NW BHJ layer. The positive photocurrent values on the real axis increased as the ZnO-NW length increased (red ∇ ; Figure 8C), and this behavior was closely related with that of J_{sc} given in Figure 2A. Characteristic features of the IMPS spectra of the solar cells were the negative photocurrent responses in the second quadrant region. The negative responses were probably caused by the electron diffusion to the Au back contact, opposing the current flow in the normal solar cell operation. The longer the ZnO-NWs became, the larger the negative photocurrent became. This was because of a decrease in the thickness of the PbS overlayer, which acted more or less as an electron-blocking layer.

We then intentionally changed the PbS deposition cycles to study the PbS-QD overlayer thickness dependence of the solar cell performance (Figure 2B). From the photovoltaic performances of the solar cells measured under 1-sun illumination, J_{sc} showed a weak PbS dependence on layer thickness, as confirmed by the IMPS spectra (Figure 8B). Unlike the IMPS spectra of the solar cells with different ZnO-NW lengths (Figure 8C), the positive photocurrent on the real axis was virtually independent of the PbS-QD deposition cycles (red ∇ ; Figure 8D), which were similar to the J_{sc} behaviors given in Figure 2B. This clearly shows that J_{sc} values were chiefly determined by the PbS-QD/ZnO-NW BHJ region (region 1) in solar cells of both types. On the other hand, V_{oc} values depended much more strongly on the layer thickness. In particular, the solar cells fabricated by 20 and 25 PbS-QD deposition cycles gave lower V_{oc} values. This was because the PbS loading amounts are not sufficient to form a flat surface, as evidenced by the SEM cross-section observations (SI Figure S2). Therefore, photo-generated electrons were considered to diffuse to the back contact easily. This is confirmed by the IMPS observations showing that negative photocurrents increased with decreasing PbS-QD deposition cycles (O; Figure 8D).

The most important finding in this series of studies is the long distance carrier transportation in the PbS-QD/ZnO-NW solar cells. Once a good electron pathway is constructed in the solar cells, holes created in the PbS-QD/ZnO-NW BHJ layer can be transported over $1 \mu\text{m}$ toward the gold back-contact (Figure 1). The formation of spatially well-separated carrier pathways is one reason for achieving long carrier transportation in the PbS-QD/ZnO-NW BHJ region. A certain charge separation mechanism is needed to form such carrier pathways. The energy offset between the bottom of the conduction band of ZnO-NWs and the lowest-lying excited state of PbS-QDs is considered to be one of the important factors. In addition to this type II energy alignment, a space charge region or depletion region, which can be formed

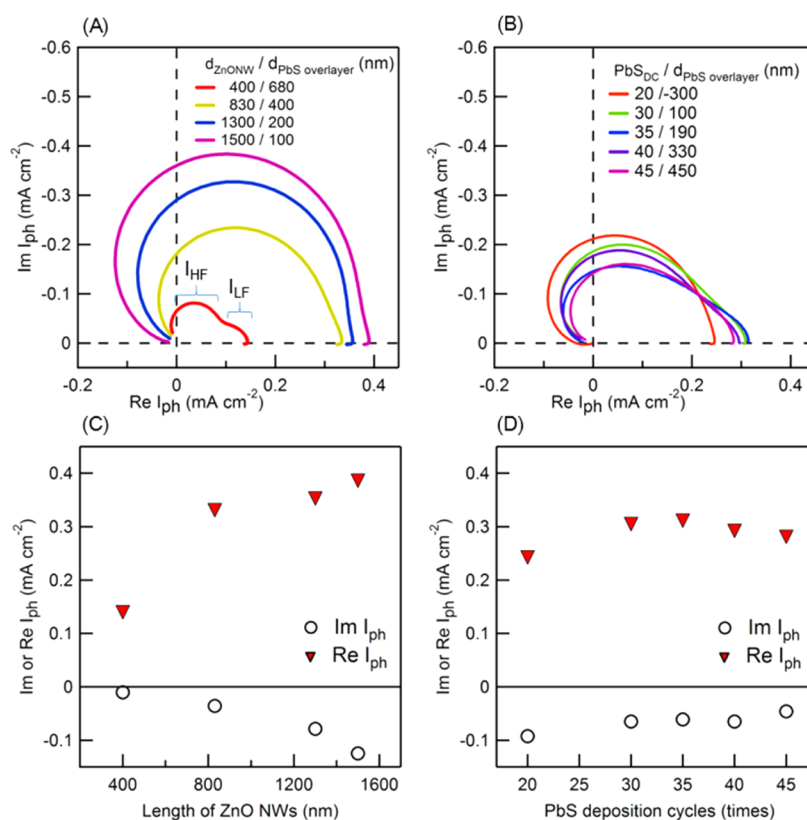


Figure 8. Intensity-modulated photocurrent spectroscopy spectra. IMPS spectra obtained on the Type A solar cells (A) and Type B (B). The maximum and minimum values of the real part of photocurrent density plotted as functions of ZnO-NW length (C) and number of PbS deposition cycles (D): the solar cell with 400 nm long ZnO-NWs shows two distinct semicircles of I_{HF} and I_{LF} (red line).

between ZnO-NWs and PbS-QDs, causes charge separation to occur.³⁴ Our experimental results indicate that once charge separation occurs inside the PbS-QD/ZnO-NW BHJ layer almost all of the electrons and holes reach the collecting electrodes. Thin PbS overlayers are convenient for avoiding gold–ZnO contact, which could result in a short circuit in the cell. However, these overlayers need to be as thin as possible to minimize the hole transport resistance and negative contributions to charge collection efficiency.

CONCLUSIONS

Colloidal PbS-QD-based solar cells yielding high EQEs in the near IR region were constructed using ZnO-NW arrays and thin overlayers. The high efficiency in the near IR region was chiefly due to the incorporation of ZnO-NW-based electron pathways in the PbS-QD layer. More importantly, the construction of separate carrier pathways led to highly efficient hole transportation inside the PbS-QD/ZnO-NW BHJ layer. V_{oc} was related to the band bending of ZnO, which determined the maximum value attainable by the solar cell.

The PbS-QD overlayer thickness dependence of the negative photocurrent observed in the IMPS spectra indicated the photo-generated electron diffusion to the Au back contact, which in turn decreased the V_{oc} and/or J_{sc} . Solar cell performance can be increased even further by depositing an efficient electron blocking layer (or hole transport layer)^{35–37} between the PbS overlayer and Au back contact. Since the exciton diffusion length in the PbS layer was a limiting parameter in solar power generation, an increase in carrier mobility of the bulk PbS-QD overlayer will contribute to improved carrier collection efficiency. Combined with recent progress in developing new

architectures,^{38–42} and durability verification,¹⁶ our experimental observations of long distance carrier transportation in PbS-QD/ZnO-NW solar cells imply the possible realization of still higher performance.

ASSOCIATED CONTENT

Supporting Information

The Supporting Information is available free of charge on the ACS Publications website at DOI: 10.1021/acs.jpcc.5b09152.

Additional cross-sectional SEM images of the cells, morphological characteristics of the cells, absorption spectra of FTO and FTO/ZnO-NW electrodes, light harvesting efficiency spectra of the cells, calculation of EQE_{PbS} , absorption coefficient of PbS calculated from equation, suggested equivalent circuit of the cells, influence of contact effects, and resistances in films (PDF)

AUTHOR INFORMATION

Corresponding Authors

*E-mail: pedro@uji.es.

*E-mail: ukubo@mail.ecc.u-tokyo.ac.jp.

*E-mail: csegawa@mail.ecc.u-tokyo.ac.jp.

Notes

The authors declare no competing financial interest.

ACKNOWLEDGMENTS

This research is supported by the Japan Science and Technology Agency (JST) through its “Funding Program for Core Research for Evolutional Science and Technology (339-5 CREST)” and New Energy and Industrial Technology Development

Organization (0520002 NEDO) and the Ministry of Economy, Trade and Industry (METI), Japan. The work is also supported by Generalitat Valenciana (ISIC/2012/008 Institute of Nanotechnologies for Clean Energies, PROMETEO/2014/020). This work is partly supported by JX Nippon Oil & Energy Corporation. Cordial thanks are due to Toyo Corporation for the use of the ModuLab system (Solartron) for obtaining IMPS data.

REFERENCES

- (1) O'Regan, B.; Grätzel, M. A Low-Cost, High-Efficiency Solar-Cell Based on Dye-Sensitized Colloidal TiO₂ Films. *Nature* **1991**, *353*, 737–740.
- (2) Huang, J.; Yin, Z.; Zheng, Q. Applications of ZnO in Organic and Hybrid Solar Cells. *Energy Environ. Sci.* **2011**, *4*, 3861–3877.
- (3) Martinson, A. B. F.; Goes, M. S.; Fabregat-Santiago, F.; Bisquert, J.; Pellin, M. J.; Hupp, J. T. Electron Transport in Dye-Sensitized Solar Cells Based on ZnO Nanotubes: Evidence for Highly Efficient Charge Collection and Exceptionally Rapid Dynamics. *J. Phys. Chem. A* **2009**, *113*, 4015–4021.
- (4) Greene, L. E.; Law, M.; Goldberger, J.; Kim, F.; Johnson, J. C.; Zhang, Y.; Saykally, R. J.; Yang, P. Low-temperature Wafer-scale Production of ZnO Nanowire Arrays. *Angew. Chem., Int. Ed.* **2003**, *42*, 3031–3034.
- (5) Krunks, M.; Dedova, T.; Oja Ačik, I. Spray Pyrolysis Deposition of Zinc Oxide Nanostructured Layers. *Thin Solid Films* **2006**, *515*, 1157–1160.
- (6) Xu, S.; Wang, Z. L. One-dimensional ZnO Nanostructures: Solution Growth and Functional Properties. *Nano Res.* **2011**, *4*, 1013–1098.
- (7) Law, M.; Greene, L. E.; Johnson, J. C.; Saykally, R.; Yang, P. Nanowire Dye-sensitized Solar Cells. *Nat. Mater.* **2005**, *4*, 455–459.
- (8) Zhang, Q. F.; Yodyingyong, S.; Xi, J. T.; Myers, D.; Cao, G. Z. Oxide Nanowires for Solar Cell Applications. *Nanoscale* **2012**, *4*, 1436–1445.
- (9) Takanezawa, K.; Hirota, K.; Wei, Q. S.; Tajima, K.; Hashimoto, K. Efficient Charge Collection with ZnO Nanorod Array in Hybrid Photovoltaic Devices. *J. Phys. Chem. C* **2007**, *111*, 7218–7223.
- (10) Carey, G. H.; Abdelhady, A. L.; Ning, Z.; Thon, S. M.; Bakr, O. M.; Sargent, E. H. Colloidal Quantum Dot Solar Cells. *Chem. Rev.* **2015**, DOI: 10.1021/acs.chemrev.5b00063.
- (11) Lan, X. Z.; Masala, S.; Sargent, E. H. Charge-Extraction Strategies for Colloidal Quantum Dot Photovoltaics. *Nat. Mater.* **2014**, *13*, 233–240.
- (12) Gonfa, B. A.; Kim, M. R.; Deegan, N.; Tavares, A. C.; Izquierdo, R.; Wu, N.; El Khakani, M. A.; Ma, D. Towards High Efficiency Air Processed Near Infrared Responsive Photovoltaics: Bulk Heterojunction Solar Cells Based on PbS/CdS Core-shell Quantum Dots and TiO₂ Nanorod Arrays. *Nanoscale* **2015**, *7*, 10039–10049.
- (13) Jean, J.; Chang, S.; Brown, P. R.; Cheng, J. J.; Rekemeyer, P. H.; Bawendi, M. G.; Gradecak, S.; Bulovic, V. ZnO Nanowire Arrays for Enhanced Photocurrent in PbS Quantum Dot Solar Cells. *Adv. Mater.* **2013**, *25*, 2790–2796.
- (14) Kramer, I. J.; Zhitomirsky, D.; Bass, J. D.; Rice, P. M.; Topuria, T.; Krupp, L.; Thon, S. M.; Ip, A. H.; Debnath, R.; Kim, H. C.; et al. Ordered Nanopillar Structured Electrodes for Depleted Bulk Heterojunction Colloidal Quantum Dot Solar Cells. *Adv. Mater.* **2012**, *24*, 2315–2319.
- (15) Wang, H.; Kubo, T.; Nakazaki, J.; Kinoshita, T.; Segawa, H. PbS-Quantum-Dot-Based Heterojunction Solar Cells Utilizing ZnO Nanowires for High External Quantum Efficiency in the Near-Infrared Region. *J. Phys. Chem. Lett.* **2013**, *4*, 2455–2460.
- (16) Wang, H.; Kubo, T.; Nakazaki, J.; Segawa, H. PbS Colloidal Quantum Dot/ZnO-Based Bulk-Heterojunction Solar Cells with High Stability under Continuous Light Soaking. *Phys. Status Solidi RRL* **2014**, *8*, 961–965.
- (17) Chang, J.; Kuga, Y.; Mora Seró, I.; Toyoda, T.; Ogomi, Y.; Hayase, S.; Bisquert, J.; Shen, Q. High Reduction of Interfacial Charge Recombination in Colloidal Quantum Dot Solar Cells by Metal Oxide Surface Passivation. *Nanoscale* **2015**, *7*, 5446–5456.
- (18) Romero, H. E.; Drndic, M. Coulomb Blockade and Hopping Conduction in PbSe Quantum Dots. *Phys. Rev. Lett.* **2005**, *95*, 156801.
- (19) Sandeep, C. S.; Cate, S.; Schins, J. M.; Savenije, T. J.; Liu, Y.; Law, M.; Kinge, S.; Houtepen, A. J.; Siebbeles, L. D. High Charge-carrier Mobility Enables Exploitation of Carrier Multiplication in Quantum-dot Films. *Nat. Commun.* **2013**, *4*, 2360–2366.
- (20) Liu, Y.; Gibbs, M.; Puthussery, J.; Gaik, S.; Ihly, R.; Hillhouse, H. W.; Law, M. Dependence of Carrier Mobility on Nanocrystal Size and Ligand Length in PbSe Nanocrystal Solids. *Nano Lett.* **2010**, *10*, 1960–1969.
- (21) Tang, J.; Kemp, K. W.; Hoogland, S.; Jeong, K. S.; Liu, H.; Levina, L.; Furukawa, M.; Wang, X. H.; Debnath, R.; Cha, D. K.; et al. Colloidal-Quantum-Dot Photovoltaics using Atomic-Ligand Passivation. *Nat. Mater.* **2011**, *10*, 765–771.
- (22) Murphy, J. E.; Beard, M. C.; Nozik, A. J. Time-Resolved Photoconductivity of PbSe Nanocrystal Arrays. *J. Phys. Chem. B* **2006**, *110*, 25455–25461.
- (23) Zhitomirsky, D.; Kramer, I. J.; Labelle, A. J.; Fischer, A.; Debnath, R.; Pan, J.; Bakr, O. M.; Sargent, E. H. Colloidal Quantum Dot Photovoltaics: The Effect of Polydispersity. *Nano Lett.* **2012**, *12*, 1007–1012.
- (24) Stadler, P.; Sutherland, B. R.; Ren, Y.; Ning, Z. J.; Simchi, A.; Thon, S. M.; Hoogland, S.; Sargent, E. H. Joint Mapping of Mobility and Trap Density in Colloidal Quantum Dot Solids. *ACS Nano* **2013**, *7*, 5757–5762.
- (25) Zhitomirsky, D.; Voznyy, O.; Hoogland, S.; Sargent, E. H. Measuring Charge Carrier Diffusion in Coupled Colloidal Quantum Dot Solids. *ACS Nano* **2013**, *7*, 5282–5290.
- (26) Kim, S.; Im, S. H.; Kang, M.; Heo, J. H.; Seok, S. I.; Kim, S. W.; Mora-Sero, I.; Bisquert, J. Air-stable and Efficient Inorganic-organic Heterojunction Solar Cells using PbS Colloidal Quantum Dots Capped by 1-dodecanethiol and Oleic Acid. *Phys. Chem. Chem. Phys.* **2012**, *14*, 14999–15002.
- (27) Etgar, L.; Moehl, T.; Gabriel, S.; Hickey, S. G.; Eychmuller, A.; Grätzel, M. Light Energy Conversion by Mesoscopic PbS Quantum Dots/TiO₂ Heterojunction Solar Cells. *ACS Nano* **2012**, *6*, 3092–3099.
- (28) Mora-Sero, I.; Bertoluzzi, L.; Gonzalez-Pedro, V.; Gimenez, S.; Fabregat-Santiago, F.; Kemp, K. W.; Sargent, E. H.; Bisquert, J. Selective Contacts Drive Charge Extraction in Quantum Dot Solids via Asymmetry in Carrier Transfer Kinetics. *Nat. Commun.* **2013**, *4*, 2272.
- (29) Park, H.-Y.; Ryu, I.; Kim, J.; Jeong, S.; Yim, S.; Jang, S.-Y. PbS Quantum Dot Solar Cells Integrated with Sol-Gel-Derived ZnO as an n-Type Charge-Selective Layer. *J. Phys. Chem. C* **2014**, *118*, 17374–17382.
- (30) Rath, A. K.; Lasanta, T.; Bernechea, M.; Diedenhofen, S. L.; Konstantatos, G. Determination of Carrier Lifetime and Mobility in Colloidal Quantum Dot Films via Impedance Spectroscopy. *Appl. Phys. Lett.* **2014**, *104*, 063504.
- (31) Tan, F.; Qu, S.; Jiang, Q.; Liu, J.; Wang, Z.; Li, F.; Yue, G.; Li, S.; Chen, C.; Zhang, W.; Wang, Z. Interpenetrated Inorganic Hybrids for Efficiency Enhancement of PbS Quantum Dot Solar Cells. *Adv. Energy Mater.* **2014**, *4*, 1400512.
- (32) Bisquert, J.; Mora-Sero, I.; Fabregat-Santiago, F. Diffusion-Recombination Impedance Model for Solar Cells with Disorder and Nonlinear Recombination. *ChemElectroChem* **2014**, *1*, 289–296.
- (33) Tena-Zaera, R.; Elias, J.; Levy-Clement, C.; Bekeny, C.; Voss, T.; Mora Seró, I.; Bisquert, J. Influence of the Potassium Chloride Concentration on the Physical Properties of Electrodeposited ZnO Nanowire Arrays. *J. Phys. Chem. C* **2008**, *112*, 16318–16323.
- (34) Mora-Sero, I.; Fabregat-Santiago, F.; Denier, B.; Bisquert, J.; Tena-Zaera, R.; Elias, J.; Levy-Clement, C. Determination of Carrier Density of ZnO Nanowires by Electrochemical Techniques. *Appl. Phys. Lett.* **2006**, *89*, 203117.
- (35) Brown, P. R.; Lunt, R. R.; Zhao, N.; Osedach, T. P.; Wanger, D. D.; Chang, L. Y.; Bawendi, M. G.; Bulovic, V. Improved Current Extraction from ZnO/PbS Quantum Dot Heterojunction Photovoltaics Using a MoO₃ Interfacial Layer. *Nano Lett.* **2011**, *11*, 2955–2961.

(36) Gao, J. B.; Perkins, C. L.; Luther, J. M.; Hanna, M. C.; Chen, H. Y.; Semonin, O. E.; Nozik, A. J.; Ellingson, R. J.; Beard, M. C. n-Type Transition Metal Oxide as a Hole Extraction Layer in PbS Quantum Dot Solar Cells. *Nano Lett.* **2011**, *11*, 3263–3266.

(37) Chuang, C. H.; Brown, P. R.; Bulovic, V.; Bawendi, M. G. Improved Performance and Stability in Quantum Dot Solar Cells through Band Alignment Engineering. *Nat. Mater.* **2014**, *13*, 796–801.

(38) Ning, Z.; Voznyy, O.; Pan, J.; Hoogland, S.; Adinolfi, V.; Xu, J.; Li, M.; Kirmani, A. R.; Sun, J. P.; Minor, J.; et al. Air-Stable n-Type Colloidal Quantum Dot Solids. *Nat. Mater.* **2014**, *13*, 822–828.

(39) Labelle, A. J.; Thon, S. M.; Kim, J. Y.; Lan, X.; Zhitomirsky, D.; Kemp, K. W.; Sargent, E. H. Conformal Fabrication of Colloidal Quantum Dot Solids for Optically Enhanced Photovoltaics. *ACS Nano* **2015**, *9*, 5447–5453.

(40) Labelle, A. J.; Thon, S. M.; Masala, S.; Adachi, M. M.; Dong, H.; Farahani, M.; Ip, A. H.; Fratallocchi, A.; Sargent, E. H. Colloidal Quantum Dot Solar Cells Exploiting Hierarchical Structuring. *Nano Lett.* **2015**, *15*, 1101–1108.

(41) Kim, S.; Marshall, A. R.; Kroupa, D. M.; Miller, E. M.; Luther, J. M.; Jeong, S.; Beard, M. C. Air-Stable and Efficient PbSe Quantum-Dot Solar Cells Based upon ZnSe to PbSe Cation-Exchanged Quantum Dots. *ACS Nano* **2015**, *9*, 8157–8164.

(42) Kawawaki, T.; Wang, H.; Kubo, T.; Saito, K.; Nakazaki, J.; Segawa, H.; Tsuma, T. Efficiency Enhancement of PbS Quantum Dot/ZnO Nanowire Bulk-Heterojunction Solar Cells by Plasmonic Silver Nanocubes. *ACS Nano* **2015**, *9*, 4165–4172.